Atmos. Chem. Phys. Discuss., 11, 23761–23800, 2011
www.atmos-chem-phys-discuss.net/11/23761/2011/
doi:10.5194/acpd-11-23761-2011

Atmospheric Chemistry and Physics Discussions

Observations and modelling of microphysical variability, aggregation and sedimentation in tropical storm cirrus outflow regions

M. W. Gallagher[1], P. J. Connolly[1], A. Heymsfield[2], K. N. Bower[1], T. W. Choularton[1], G. Allen[1], M. J. Flynn [1], G. Vaughan[1], and J. Hacker[3]

[1]Centre for Atmospheric Science, University of Manchester, Manchester, UK
[2]NCAR, P.O. Box 3000, Boulder, CO, 80307-3000, USA
[3]School of the Environment, Flinders University, GPO Box 2100, Adelaide 5001, Australia

Received: 28 July 2011 – Accepted: 10 August 2011 – Published: 22 August 2011

Correspondence to: M. W. Gallagher (martin.gallagher@manchester.ac.uk)

Published by Copernicus Publications on behalf of the European Geosciences Union.

Abstract

Aircraft measurements of the microphysics of a tropical convective anvil (at temperatures $\sim -60\,^{\circ}C$) forming above the HECTOR storm have been performed. The observed microphysics has been compared to a bulk and explicit microphysical model of the anvil region including crystal aggregation and sedimentation.

It has been found that in flights made using straight and level runs perpendicular to the storm that the number of ice crystals initially decreased with distance from the storm as aggregation took place resulting in larger crystals followed by their loss due to sedimentation. At still greater distances from the storm the number of very small crystals increased. This is attributed to the formation of new ice crystals on aerosol particles as the ice super saturation rose following the depletion of the larger ice particles following aggregation and sedimentation. Comparison with the explicit microphysics model showed that the changes in the shapes of the ice crystal spectra as a function of distance from the storm could be explained by the explicit microphysical model if the aggregation efficiency was set to $E \sim 0.02$.

It is noteworthy that this aggregation efficiency is much larger than values normally used in cloud resolving models at these temperatures (typically $E \sim 0.0016$). Furthermore if the bulk model is used then optimum agreement was reached with a collection efficiency for aggregation of $E \sim 0.05$. These results are important for the treatment of the evolution and lifetime of tropical cirrus clouds.

1 Introduction

The response of the tropical atmosphere to changes in climate forcing has received much attention lately (IPCC, 2007) since a positive feedback, arising from increased supply of water vapour by convection in the tropical tropo-pause layer (TTL), may be countered by negative feedbacks due to increasing amounts of thin cirrus clouds also being formed in this region. These cloud types have been identified as a significant

ACPD
11, 23761–23800, 2011

source of uncertainty in the Earth's radiation budget (Lynch et al., 2002) with several recent studies showing that their contribution to the earth-atmosphere radiation and water budgets in the TTL can be very significant, (Edwards et al., 2007; Stephens et al., 2002; Liou et al., 1994; Donner et al., 1997). Many studies show that optically thin cirrus are prevalent in the region of the tropical tropopause: (McFarquhar et al., 2000; Massie et al., 2002; and Dessler et al., 2006) and recently it has been suggested that this frequency, and hence radiative contribution may be larger than hitherto assumed, (Lee et al., 2009). Furthermore, analysis of several large cloud microphysical data sets, Baum et al., (2005), when compared with MODIS simulated retrievals, have revealed differences between in situ and retrieved single scattering albedo and asymmetry parameters. These differences were found to be largest for ice clouds formed in areas of deep convection (e.g. the TRMM-KWAJEX project) compared to those formed in regions of low updraft velocities. Compared to other cloud types there are relatively few measurements of ice crystal particle size distributions (PSD) in those formed through tropical deep convection. It is known, Fusina et al. (2007) that depending on conditions, the transition between net warming and cooling due to cirrus depends on ice PSD. Hence, there is a general need to determine ice PSD within cirrus to allow better analysis of their mean radiative impacts and potential feedbacks. To reduce uncertainties in cloud model radiative predictions in these regions more and improved data sets of PSD are needed, particularly for high level cirrus. In general previous studies have focused on two different types of cirrus cloud; thin semi-laminar cirrus associated with in situ formation by synoptic and mesoscale processes, and those originating from deeper convection in mid-latitudes. Here we present a typical case study of the microphysical variation observed within cirrus generated in tropical storm anvil outflow.

2 Background

Tropical anvil cirrus form at the top of deep cumulonimbus clouds, consisting initially of ice "debris", that spreads out laterally from the convective storm cells, with the larger

ACPD
11, 23761–23800, 2011

ice particles being removed rapidly by sedimentation. Aggregation and sedimentation then dominate ice removal in the anvil downwind of the convective centre. In the tropics these anvils give way to new in situ generated cirrus at the tropical tropopause and form extremely widespread cloud layers of several hundreds to thousands of km in extent, thus contributing to large-scale radiative effects (Collins et al., 1996). The prevalent conceptual model of in situ generated cirrus has been well described by Heymsfield and McFarquhar (2002) in which three distinct layers are identified. This conceptual model was based originally on in situ cirrus ice particle size distribution measurements made during the FIRE-I experiment, e.g. Gultepe and Starr (1994), using aircraft Lagrangian spiral descents and in the FIRE-II experiment using balloon-borne ice crystal replicators (Miloshevich et al., 1992). It was observed that average ice crystal sizes increased steadily from near cloud top towards cloud base. From the observed vertical distribution of ice crystal PSD and detailed photographs of their habits it was inferred that these cirrus can be represented, conceptually, by the following three layers with broadly distinct characteristics:

Layer 1 – The Nucleation layer in the uppermost part of the cloud is composed of small ice crystals, or proto-crystals, typically proto-bullet rosettes. In this layer ice production occurs when the relative humidity (RH) exceeds some critical value necessary for ice activation. Ice crystals in this layer are often up to a few tens of micrometers in size;

Layer 2 – The Growth layer which is much thicker and comprised of ice crystals which present pristine habits due to sufficient ice super-saturation (S_{ice}) that allows sustained ice crystal growth to large sizes, typically several hundreds of microns in length, but sometimes exceeding 1–2 mm;

Layer 3 – The Sublimation layer where conditions of ice sub-saturation (S_{ice} i 1) cause sublimation and eventually complete evaporation of the ice crystals falling from the layer above. In this layer ice crystals often present as rounded forms and are more difficult to classify than those in layer 2. The thickness of layer 3 depends on the ice water content (IWC) and the PSD near the base of layer 2 as well as the RH and temperature

ACPD
11, 23761–23800, 2011

(T) profiles below layer 2.

How anvil cirrus transition, and the spatial scales over which the transition occurs are important. Near the base of deep anvil cirrus, layer-2 observed ice crystal size distributions should be dominated by aggregation processes but the extent to which new ice particle nucleation and growth contributes to the outflow structure has not been examined in detail, particularly the interaction with environmental air in the lateral wings of the anvil region. If we consider the *nucleation layer* there is evidence from controlled cloud chamber studies replicating conditions near the TTL, that the singular freezing hypothesis explains the homogeneous ice nucleation process associated with particle formation, Möhler et al. (2007) (although depending on the vertical velocity and actual temperature profile, the nucleation could be either discrete or stochastic). In this case polycrystal habit formation will occur presenting as simple pristine bullet rosettes or hexagonal plates. The initial anvil cirrus at and near the top of a cumulonimbus outflow however presents larger ranges and variations due to the influence of aggregation following heterogeneous ice nucleation in the convective cell up-draughts. However, it is very difficult to sample these regions in situ with sufficient detail: Takahashi et al., 1995; Boussatson et al., 2004.

Based on this observationally driven conceptual model we expect significant vertical variation in IWC and PSD through such cirrus layers, however, we must also anticipate that significant lateral variation in the cirrus properties will occur, particularly in relatively thin layer cirrus produced by smaller convective storms due to interaction of the initial large-scale vertical motion with the tropical tropopause layer (TTL) and subsequent spreading into the background environmental air. The conceptual cirrus model has largely been confirmed in many recent studies of cirrus formed in low updraught regions, e.g. frontal cirrus in the sub-tropical UTLS, e.g. during the EMERALD project, e.g. Gallagher et al. (2002) and in tropical cirrus during the Tropical Warm Pool-Ice Characterisation Experiment (TWP-ICE), conducted in Darwin, McFarquhar et al. (2008). The number, extent and even presence of these conceptual layers, however, can vary significantly during the evolution of tropical deep convection generated

ACPD
11, 23761–23800, 2011

cirrus. Furthermore, the transition from the immediate anvil cirrus to that produced by in situ generation zones downwind of the storm is complex and the variation in microphysical properties in the horizontal lateral flow within these interacting zones is likely not fully resolved by large scale models.

3 Tropical storm outflow

The structure of thunderstorm outflow anvils has been discussed extensively, e.g. Lilly (1988), and is often described as a two-stage process. The initial outflow region is analogous to a wake collapse phenomenon with the addition of differential heating provided by infra red radiation, whereby an approximately uniformly buoyant cold air intrusion into a stably stratified layer takes place. Vertical constraint of the intruding plume by the local environmental stability leads to its external collapse. The wake formed by the collapsing intruding plume flattens and spreads horizontally, the expansion slowing as the flow stabilises. Internal collapse of the near isotropic turbulence within the plume also leads to transformation of turbulent energy into larger scale wave motion dominated by two-dimensional turbulence as the plume flattens. However, much of the uncertainty in models of storm outflow development and influences on radiative forcing centre on whether the subsequent mixed layer can fully develop before most of the ice within it has precipitated out, Lilly (1988). Star and Cox (1985) suggest precipitation is important for the plume development and radiative heating impact, reducing the optical path and hence radiative effect. However it can also produce below cloud evaporative cooling maintaining downward growth, (an effective dehydration mechanism) Danielson (1982), but reducing turbulent energy generation. The differential radiative heating profile in the developed plume can subsequently drive convection in the thin cirrus layer downwind, by maintaining or regenerating turbulence.

ACPD
11, 23761–23800, 2011

4 Description of experimental flights and tropical storm environment

We present in situ airborne microphysical measurements conducted as part of the ACTIVE experiment, during a typical "Hector" deep convective storm which forms over the Tiwi Islands (Bathurst and Melville Islands), to the North of Darwin, Australia (12.47° S, 130.85° E). The case presented (AE13) is from 9 December 2005, which is during the Austral summer and the pre-monsoon-monsoon break period for that region. The meteorological, as well as regional climate, context of the experiment in which this case study was conducted is comprehensively described by Vaughan et al. (2008). A statistical analysis of the thermodynamic characteristics of Hector storms in this region during this period can also be found in May et al. (2009). The ACTIVE experiment was explicitly designed to study the transport of water vapour, aerosols and chemicals into the tropical upper troposphere and lower stratosphere (UTLS) focusing on the inflow and outflow of deep tropical convective systems as a mechanism generating this transport. However, in situ cloud microphysical measurements were also conducted to delineate the anvil cloud extent and to place new aerosol particle nucleation processes in context. The full experimental design, the study region and details of the aircraft platforms as well as the instruments used are described in detail by Vaughan et al. (2008).

During flight AE13, Hector storm anvil cirrus presented between 11.5 and <17 km altitude. A series of penetrations were made by the ARA high altitude Egrett aircraft between 14:30 and 17:00 local time during the anvil development. Penetrations were conducted perpendicular to the storm outflow region and confined to a near constant altitude, 13.0–13.25 km, with average temperatures of −58 °C. This represents mainly the base of the supersaturated layer, 2, discussed above. Analysis of cloud microphysical variation focused mainly on data collected during four N-S tracks, labeled 1–4 in Fig. 1. These penetrated the outflow at increasing distances from the Hector storm centre both perpendicular to and parallel to the centre-line of the outflow. The penetrations occurred at distances between 19 and 93 km from the storm centre and are

ACPD
11, 23761–23800, 2011

summarised in Table 1. This outflow survey region covered approximately 1.2° of longitude and 0.7° of latitude. Lengths of individual penetrations ranged from ∼120 to ∼140 km. Winds measured by the aircraft at the sampling altitude were reported to be constant, Easterlies at 15-20 $m\,s^{-1}$ whilst in the inflow region of the storm, NE of the islands, the flow was reported to be approximately NE. The observations here represented cirrus ages ranging from 1–3 h subsequent to storm initiation.

The Hector storm and its development on this day is shown in the corresponding MTSAT-IR images in Fig. 2a–d centered on the Darwin study region. Brightness temperatures for cloud top height (CTH), in this region were retrieved following the methods described by Allen et al. (2009). Examination of the brightness temperature variation through this sequence of images revealed evidence of gravity waves propagating to the West and SW of the storm centre as highlighted in Fig. 2c. There is also evidence of some convective regeneration leading to convective turrets, also highlighted, within the anvil outflow. This may influence the subsequent analysis to some extent, which is described below. One of the noteworthy features of the outflow on this occasion is the large scale horizontal wave structure in the outflow leading to transverse asymmetry in the delineated anvil cirrus. Towards the end of the experiment a second weaker storm developed to the south over Charles Point and the Beagle Gulf, to the West of Darwin but the outflow cirrus there remained separate from Hector.

4.1 Instrumentation

The instruments used to determine the cirrus bulk and microphysical properties in this study were; a Cloud Particle Imaging (CPI) probe (Model Version 003, Stratton Park Engineering Company, SPEC, USA), (see e.g. Lawson et al. 2006a); a Cloud-Aerosol-Precipitation-Spectrometer (manufactured by Droplet Measurement Technology, DMT), described by Baumgardner et al. (2007); and a Cloud Droplet Probe (CDP-100, Version 1, DMT). The CAPS instrument is a so-called multi-probe containing a 2D Cloud-Imaging Probe (CIP-25), capable of imaging ice crystals in the size range (25–1575 µm), a Cloud Aerosol Spectrometer (CAS), a Mie scattering forward scattering

ACPD
11, 23761–23800, 2011

spectrometer probe designed to measure droplet PSD between 0.6–50 µm and a hot-wire liquid water content probe. In this work we focus mainly on ice crystal images reported by the CPI and ice water content (IWC) and PSD measurements made by the CAPS.

The SPEC CPI probe records 256 level grey scale CCD images of ice crystals with dimensions in the range 10–1800 µm. An algorithm was developed to correct for over sizing due to particles lying outside the depth of focus of the instrument and for quantifying the probe sample volume, which is particle size dependent, as described by Korolev (2007) and Connolly et al. (2008). Sample volume may also depend on other factors such as inefficiencies in the particle detection and camera triggering system due to misalignment although this can be overcome by operating the instrument in the absence of the detection system and using so-called "continuous trigger" mode whereby the camera is allowed to "free-run". The inherent resolution of the CCD camera (2.3 µm) in the CPI limits the accuracy of habit identification to particles with dimensions greater than ~40 µm in size. Whilst capable of providing high resolution 256 grey scale images of ice particles, useful for identifying ice crystal habits, the major limitation of the CPI is its sample volume size, which is typically ~0.47 l s^{-1} (maximum) compared to the CAPS and similar 2D imaging probes which are typically ~>5 l s^{-1}. This necessitates integrating CPI PSD measurements over typically 10 second periods in most cirrus conditions. However, in conditions when very low concentrations of large ice crystals occur (sizes greater than a few hundred µm), averaging times of minutes may be required to reduce statistical counting errors to acceptable levels, see e.g. Baran et al. (2009). To overcome this we us the CAPS-CIP instrument which affords 1 Hz PSD and IWC although for this study 5 second integrations were used. The corrected PSD's, when averaged over individual flight tracks, were found to be in good agreement between the two instruments, Fig. 3.

ACPD
11, 23761–23800, 2011

4.2 Data analysis and uncertainties

Ice water contents were computed from the CAPS CIP PSD, integrated typically over 5 seconds, assuming an effective ice crystal density, ρ_e, and using the habit dependent mass-dimensional relationship, described by Heymsfield (2004). This is of the form $m(D) = 3.4709D^{2.6}$ where D is the maximum particle dimension. These relationships are described in detail together with the ice crystal classification criteria and methods for calculating ice masses by Heymsfield et al. (2002, 2004) and are summarized for crystal habits relevant to other imaging probes (e.g. CPI) described by Baran et al. (2009). In addition, seven ice crystal classification criteria were used to analyse the CPI particle images and are incorporated in analysis software developed by SPEC, Inc., (Lawson and Baker, 2006a,b). The individual classifications and criteria are summarized in Baran et al. (2009) along with the associated equations for mass calculation. These were used to classify the habits types at different points in the cloud, e.g. cirrus bullet rosettes are relatively easy to distinguish, however here we will focus mainly on the observed PSD reported by the CIP as we are mainly interested in the aggregation zone where most particles presented as aggregates of hexagonal plates.

To identify significant spatial changes in microphysical behaviour the ice crystal PSD were parameterised using a simple exponential model distribution, Eq. (1), e.g. Field et al. (2007). In this simple parametric equation, N is the ice crystal concentration, D the maximum crystal dimension, n_o is the intercept term, and λ_o is the slope parameter which describes the contribution to the particle population by large ice crystals (μ_Γ is the width of the distribution).

$$\frac{dN}{dD} = n_0 D^{\mu\Gamma} \exp(-\lambda_0 D) \quad (1)$$

CIP size distributions were again used to produce estimates of IWC through the mass

ACPD
11, 23761–23800, 2011

vs size relation suggested by Heymsfield (2004):

$$\mathrm{IWC} = \sum_{1}^{N} N_i \alpha D_i^{\beta} \tag{2}$$

where N_i is the concentration in bin i, $\alpha = 3.4709$ is the multiplier of the mass-size relation, D_i is the mid-point diameter of bin i, and $\beta = 2.6$ is the index in the mass size relation.

Recent studies combining ensemble cirrus models with ice PSD schemes have been able to broadly predict IWC levels, ice water profile (IWP), total solar optical depth, volume extinction coefficients and radiative properties that compare well with those derived from in situ observations, in some cases without the need for information on ice crystal effective dimension, Baran et al. (2009). However, the uncertainties associated with in situ observations from 2-D imaging spectrometers can be large. The magnitudes of these uncertainties, whilst theoretically the same for most instrument types, can vary depending on the type, configuration and incept date of the instruments which are constantly being improved.

Uncertainties associated with ice PSD measurements include limited sample volumes (e.g. the Cloud Particle Imager, Lawson et al., 2006a), insufficient grey scale information to correct for depth of focus mis-sizing (e.g. CAPS-Cloud Imaging Probe, Baumgardner et al., 2006) probe dead time, probe triggering efficiency (particularly for small particles) and random collection within the instruments depth of field (Korolev et al., 2006; Connolly et al., 2007). More seriously they can be subject to artifacts, particularly in the small, sub 50 µm size range, due to ice particle shattering on aircraft as well instrument surfaces, which has been demonstrated to be an issue for all such instruments, Korolev (2009). These artifacts appear to manifest particularly in the presence of significant concentrations of large ice crystals (typically > 4 mm). These measurement limitations are still being addressed and steps to minimize them are being generally adopted and depend on both operational, instrument and environmental conditions (Korolev, 2009; Field et al., 2006; Heymsfield, 2007) but they will continue to

ACPD
11, 23761–23800, 2011

add to the general uncertainty associated with all such in situ measurements of small ice particles for the foreseeable future. The work by Korolev (2010) suggests the CIP, and similar instruments despite being open path instruments, also suffer from ice shattering artifacts. There has been little quantitative information published on the effect particle shattering has on the CPI.

For the analysis of the ACTIVE experimental data presented here the main assumption is that particle shattering, at least for the ARA aircraft platform, and the instruments used (CPI and CAPS-CIP), will be limited to particles <50 µm which will have a small influence on the total IWC. This assumption is justified having been demonstrated by a detailed analysis of data from an similar CAPS-CIP and CPI instruments flown on the DoE Proteus aircraft as part of the TWP-ICE experiment, Mc Farqhuar et al. (2008). The TWP-ICE experiment was conducted simultaneously with the ACTIVE experiment and flights were often conducted jointly by the two aircraft, and which flew near identical cloud instruments (comparisons between the aircraft are being reported elsewhere).

Figures 3 and 4 demonstrates a typical comparison between the open-path CAPS-CIP instrument on the Egrett (which is assumed to be less prone, but not immune, to shattering artifacts) and the inlet based CPI (assumed to be more prone). The latter instrument, however, appears to be less sensitive (at least for the conditions reported here) to this artifact, likely due to limited triggering efficiency of its detection system for small particles. It should be noted that the data in this figure have been integrated across a full cloud penetration (10 min) to improve sampling statistics and so cover a wide range of PSD conditions. Figure 3 also shows the PSD measured by an open path Mie scattering spectrometer (DMT Cloud Droplet Probe, CDP-100 Version 1–2004, designed for sampling water PSD) mounted directly below the CAPS-CIP instrument, which again, considering the very different operating principles and resolutions, is encouraging, although there is a suggestion that both CIP and CPI overestimate concentrations below 50 µm. It is known that version 1 of the CDP suffers from undercounting issues for particle concentrations above approximately 200 cm^{-3}, in water clouds, Lance et al. (2010). These concentrations are much larger than reported in ice clouds.

ACPD
11, 23761–23800, 2011

Differences between the CPI and CIP reported concentrations can, however, become more pronounced on shorter sampling timescales depending on the PSD mode size. It is clear from these comparisons that for the conditions typically encountered during ACTIVE the CPI measured PSD also become statistically limited for particle sizes >800µm whereas the coarser resolution afforded by the CAPS-CIP (15 µm) will add to its uncertainties for small particles. We will expect the CPI PSD to be statistically less reliable for particle dimensions D >100 µm if using <1 min integration periods compared to the CAPS-CIP and this limitation was mitigated in the subsequent analysis by optimizing the integration time for the CPI. The effect of these different probe issues on uncertainty in deriving values of λ_o is highlighted below.

5 Results – microphysical horizontal structure variability

The spatial variation in observed PSD characteristics within the outflow region was investigated by examining the time histories of IWC (g m^{-3}) and λ_o (cm^{-1}) across each track along with the ice crystal habits presented by the CPI images as a function of increasing downwind distance, and transverse to the outflow. Figures 5a–d and 6a–d show IWC and λ_o respectively, for each flight leg (1–4) as a function of latitude, and increasing distance), plates (a)–(d), from the storm centre. Figure 5, shows a general decrease in IWC with increasing distance due to ice loss by aggregation and sedimentation. Figure 6 shows show there is a general decrease in λ_o with distance from the storm, again due to the effects of aggregation on the evolving PSD although there was significant variability.

Figures 5 and 6 suggest that there is a significant lateral shift in the core outflow region due to large-scale horizontal perturbation. Indeed there may have been two distinct outflow regions generated. To account for this when comparing with model predictions later we have computed average values of IWC and λ_0 within ±0.2° of latitude of the central outflow region to the south, and take the core region as being represented by the peak in the IWC. This peak was also confirmed by the CPI measurements. As

ACPD
11, 23761–23800, 2011

shown later this region was dominated by large aggregated ice crystals and the averaged values should be relatively unaffected by other processes such as re-nucleation which appears to occur and contribute to a greater extent in the wings of the observed outflow, as discussed later.

Flight leg 1, 19 km from the storm centre, displayed the highest IWC's, with median values $>1\,\mathrm{g\,m^{-3}}$ across the central outflow region although with low values of n_o (not shown). Thus small ice crystal concentration contributions (at least within the detection limits of the instruments) appear to contribute very little to the overall PSD here as shown by λ_o. The PSD in this region were clearly dominated by large complex aggregates comprised mainly of hexagonal plates. These large aggregates eventually sediment out downwind of the storm in the core region as can be seen by the changes in λ_o with distance. In the lateral edges of the outflow there is some evidence that λ_o (and n_o) increases as nucleation occurs. Most of the core region ice appears to have been precipitated within a distance of 30 km. Within track 2, IWC's peaked at $>1\,\mathrm{g\,m^{-3}}$ but showed greater variability. n_o (not shown) remained reasonably consistent across the outflow (albeit with small scale regions where significant enhancements occurred) as did values of λ_o downwind of the outflow. λ_o did show enhancement in several regions within track 4. In these regions the PSD were dominated by higher concentrations of small, recently formed, pristine ice crystals, which presented as small poly-crystals, or proto-bullet rosettes in some regions.

5.1 Habit variation

Images of the ice crystals recorded by the CPI corresponding to each flight leg are now considered in more detail. These are plotted in Figure 7a–d for each successive flight leg. The images are presented in a matrix plotted as a function of latitude (°) along the horizontal axis, and which has been split into 5 latitudinal bands of approximately 0.2° width, while the vertical axis shows the ice crystals sorted according to size. The distance from the storm outflow increases from Fig. 7a to d. If we inspect the wings of the outflow there is evidence in most, but not all cases, of a gradual transition to a

ACPD
11, 23761–23800, 2011

region where significant new ice particle production or re-nucleation is occurring likely due to an increase in super-saturation and subsequent haze freezing. The habit of the ice crystals in these transition regions is very different to those in the centre of the outflow, presenting as small polycrystalline or proto-bullet rosettes which are clearly imaged by the CPI, most of which are <100 µm, although some have grown to significant sizes having fallen from higher in the cloud. However these crystals appear to have undergone very little, if any, aggregation. The patterns and extents of these zones are particularly evident in the later legs, Fig. 7b to d. It is interesting that although the overall concentration of large aggregates decreases they still persist even as far downstream as track 4, some 134 km, although overall λ_o decreases.

Figure 8, shows the ice crystal size distributions, again displayed in matrix form, showing the variation within the along-axis outflow region (±0.2° latitude) for three of the penetrations at 19, 31 and 67 km downwind of the storm. The reduction in large aggregate contributions after 20 km becomes clear, leading to a gradual decrease in IWC.

If we consider the main processes governing new nucleation of ice particles in the anvil environment then key to this will be the precipitation of the larger aggregates that results in an increase in ambient ice super-saturation in the depleted region, subsequently allowing ice nucleation by haze freezing. This would lead to both an increase in n_o in such regions coupled with eventual recovery in λ_o through further aggregation. These particles, again due to the increased super-saturation, eventually grow into larger bullet-rosettes that are more characteristic of mature cirrus e.g. as seen in frontal cirrus. Figure 9 shows detailed images of the complex chain aggregates of hexagonal plates observed in this anvil outflow which should be compared with the pristine ice crystal habits (mainly large bullet rosettes) recorded in typical frontal cirrus, Fig. 10. (These were observed over Adelaide, Australia, during the EMERALD-1 experiment, Whiteway et al., 2004; Gallagher et al., 2005).

Observations within tropical anvil clouds have noted many aggregates of ice crystals, often formed in chains, Connolly et al. (2005). It is thought that a large majority of

ACPD
11, 23761–23800, 2011

these aggregates originate within the storm, where temperatures are high enough for the cohesive properties of ice to be favourable. It is also thought that aggregation of the ice crystals may be enhanced by the electric field that is present due to the charge separation mechanism in thunderstorms. Davis (1964) calculated that gravitational settling would be the dominant collision mechanism for two conducting spheres, charged or uncharged, of mass similar to that of a typical cloud particle. Saunders (1975) hypothesized that the electric field may enable two ice crystals to come together for long enough for them to sinter.

Observations from the ACTIVE project also show clear evidence of larger aggregates occurring downwind of the main area of convection of the Hector thunderstorm, thus suggesting that significant aggregation may occur within the cirrus itself. The temperature of the cirrus investigated was approximately −60 °C but it was previously thought that aggregation would not be very efficient at these temperatures. If significant aggregation does occur at these temperatures it is important to quantify as it may be an important contributory mechanism in determining cirrus lifetime. Also worthy of mention, but not wholly relevant to this study was the fact that, on occasion in localised regions, bullet rosette type crystals were also observed in the outflow cirrus. It is thought that the bullet rosette crystals form in situ, as in high level frontal cirrus, either by heterogeneous nucleation of ammonium sulphate aerosol or homogeneous freezing, Abbatt et al. (2009), and that two main criteria are necessary for their formation: (i) the cirrus has to become relatively thin, due to the fall out of larger aggregates and (ii) some reasonable uplift must be present, e.g. due to the presence of gravity waves.

6 Model Studies

The evolution of the ice crystal PSD's within the axial region of the anvil outflow was simulated using an explicit bin-aerosol-ice-microphysical model, based on the ACPIM (Aerosol Cloud Interaction Model). A description of the original model can be found

ACPD
11, 23761–23800, 2011

in Connolly et al. (2009, 2010) so only the key features relevant to this study will be repeated briefly here. The model incorporates an aerosol and cloud particle moving centre multi-bin structure developed by Jacobson et al. (1994) with mass conservative, explicit liquid-ice, ice-ice collision, coalescence, riming and aggregation processes. Aggregation is described with the stochastic collection equation (see Pruppacher and Klett, 1997), and was solved using the algorithm described by Bott (2000). The kernel applied was the gravitational kernel described by Hall (1980)

$$k(x,y) = E\frac{\pi}{4}(x+y)^2|u(x)-u(y)| \quad (3)$$

where $x$and y are the diameters of two particles, $u(\ldots)$, is the terminal fall speed verses diameter relationship and E is the aggregation efficiency - assumed to be a constant in this study –, which is the product of the collision efficiency and the sticking efficiency. The ice mass-size relation used in the model follows Heymsfield et al. (2004) for consistency with the way the CPI and CIP observational data were treated as described above, viz $m(D) = 3.4709\,D^{2.6}$ with m in kg and D in metres. Coalescence efficiencies in the model rely on experimental data from Low and List (1982) and Lew and Pruppacher (1983), and CFD calculations based on the work of Wang and Ji (1992).

Condensation is treated explicitly in the model whilst ice crystal growth and habits are treated using the model of Chen and Lamb (1994). The bin-microphysics model uses a 4th order monotonic advection and flux method for solving stochastic collision efficiencies for all bins. Ice nucleation can be represented in several different ways, either using the singular freezing hypothesis approach, using the equations described by Connolly et al. (2009), or a traditional stochastic nucleation approach. However, here we will focus on the process of aggregation and its sensitivity to the aggregation coefficient within the axial region of the anvil outflow. We assume contributions to the evolution of the PSD due to other processes in this core region, such as new particle nucleation, will be a minimum. The model was run in both bin and bulk modes and compared with observations. Finally we investigate the contribution of sedimentation to the results.

ACPD
11, 23761–23800, 2011

6.1 Model initialisation

The model was initialised with the observed thermodynamic profiles and ice water contents from the CIP. Anvil cloud thickness was based on a combination of aircraft data, cloud top heights derived from MTSAT-1R (retrieved hourly resolution data provided by P. Minnis, personal communication, 2006, 2010) and radar observations, described by May et al. (2009). The simple conceptual model described earlier was adopted by assuming uniform ice saturation (within layer 2) with a below cloud sub-saturated layer. Ice crystal PSD predictions were selected from the model levels corresponding to the aircraft cloud penetrations (13 km) and exponential gamma functions were fitted to them conserving all three moments. The ice crystal aggregation efficiency was varied between $E = 0.005$ and 0.02 and the results compared with the in situ aircraft measurements.

We assume that the case study can be considered as a Lagrangian one. The sampling times and wind speeds for each leg with a corresponding distance downwind from the first leg were determined to be: Leg 1: ~15:10; Leg 2: ~15:31, 12 km down wind, ~10 m s^{-1}; Leg 3: ~15:57, 50 km down wind, ~24 m s^{-1}; and Leg 4: ~16:15, 75km down wind, ~24 m s^{-1}. The actual horizontal wind speed at the altitude of observation was ~20 m s^{-1}in the direction the anvil outflow, whereas the assumption that the flight is Lagrangian would necessitate velocities between the legs of 10, 24 and 24 m s^{-1}. Thus it can be seen that the flight is not strictly Lagrangian; however, another simplifying assumption is that the cloud was approximately steady-state, at least on the time scale of the observations, so that the important variable is, therefore, distance downwind of the first flight leg.

6.2 Model results

The size distributions measured by the CIP instrument and a mass vs size relation, Heymsfield (2004), were used to produce estimates of IWC using: $\mathrm{IWC} = \sum_{1}^{N} N_i \alpha D_i^{\beta}$

ACPD
11, 23761–23800, 2011

where N_i is the concentration in bin i, α=3.4709 is the multiplier of the mass-size relation, D_i is the mid-point diameter of bin i, and $\beta = 2.6$ is the index in the mass size relation. To ease the analysis of the particle size distributions we also calculated moment-conserving exponential function fits to the size distributions, $\frac{dN}{dD} = n_0 \exp(-\lambda_0 D)$. The moments that were conserved were the 0th and 2nd moments, since we were interested in conserving particle number (as aggregation is a sink for number) and also mass (which for ice crystals is approximately proportional to the second moment). It can be shown that such a moment conserving fit is provided by:

$$\lambda_0 = \sqrt{2M0 / M2} \tag{4}$$

and

$$n_0 = M0 \times \lambda_0 \tag{5}$$

where M_0 and M_2 are the 0th and 2nd moments of the size distribution. These data were separated into flight legs, varying in latitude, as discussed previously, and the properties were plotted.

Figure 11a shows the IWC calculated as a function of distance from the main storm; and 11b shows λ_o as a function of distance compared to the model predicted values as a function of aggregation efficiency, E. The model predicts that IWC decreases with distance from the storm as observed, with λ_o decreasing from 9000 m^{-1} to 7000 m^{-1}, which is equivalent to a mean particle size change of 110 to 142 µm.

When compared with the stochastic collection equation we find that an aggregation efficiency of $E = 0.02$ gives the best agreement with the measurements, however, when compared with a 2 moment bulk scheme (not shown) we find $E = 0.05$ gives the best agreement. This is due to numerical diffusion in the bulk scheme arising from misrepresentation of the size dependent ice crystal fall speeds as described by Milbrandt et al. (2010).

ACPD
11, 23761–23800, 2011

6.3 The influence of sedimentation

To examine the influence of sedimentation the model was run in 1-D with sedimentation included, using 100 levels each with a vertical grid spacing of $\Delta z = 30$ m and a time step $\Delta t = 10$ s. The advection scheme used was the monotonic 4th-order polynomial interpolation scheme described by Bott (1991). The vertical wind was specified to be zero and crystals were specified to fall according to the mass-velocity relation: $v(D) = 5.73 \times 10^3 D^{1.27}$. This was determined by application of the Heymsfield et al. (2002) parameterisation to the CPI images. The mass-size relation was specified again from Heymsfield et al. (2004). The initial conditions were for ice saturation at all levels, and an exponential distribution of ice crystals above 11 km m with a mass of 1.15 g kg^{-1} and a concentration of $\sim$1600 l^{-1}.

An example of the model output for $E = 0.1$ is shown in Fig. 12. It can be seen that the concentration of ice crystals reduces throughout the simulation (due to aggregation) and is highest at the top of the cloud because of the lack of large particles to collect and remove the small particles, Fig. 12a. The ice mass-mixing ratio (IMR) also decreases with time as the larger particles, which contain most of the mass, sediment out, Fig. 12b. There is a general trend for λ_o to decrease with time initially, due to aggregation; however, once the majority of the large particles sediment out λ_o starts to increase again, which is due to the fact that the smaller particles are preferentially retained.

Figure 13a shows a comparison of measured IWC with the sedimentation model at the level of the aircraft observations. It can be seen that the ice mixing ratio decreases in the sedimentation model, as in the observations, with $E = 0.075$ giving perhaps the best agreement overall. However, the best agreement in the *change of the slope with distance* from the storm is actually for $E = 0.02$, again, initially. However at distances greater than 30 km the model is unable to produce the correct change in the slope of the distribution. This deviation is due to the effects of differential sedimentation and the assumption that the size distribution of ice crystals is initially uniform in the vertical.

ACPD
11, 23761–23800, 2011

7 Discussion

We believe that a collection efficiency of $E = 0.02$ provides the best agreement with the observed data in this case. The parcel model used showed good agreement with the measured change in the slope of the distribution with increasing distance from the storm, but was overly simplistic as the ice-mixing ratio was unable to decrease in the manner shown by the observations. The 1-D layer model, able to capture the sedimentation process, showed that at distances greater than 30 km from the storm, the effects of size dependence on the sedimentation of ice crystals is appreciable in affecting the slope of the distribution at any particular level, but at distances closer than this was able to explain the observed change in the slope well. It is difficult to adequately model the exact case conditions since we do not have data to tell us the variation of the ice crystal size-distribution with height at the initalisation time in the model. For instance if there was less ice mass aloft then this could also explain the rapid change in ice mixing ratio with distance from the storm. Similarly if the cloud were deeper than is assumed here this could reduce the increase in λ_o with distance after 30 km.

Another area of uncertainty is in the assumption of the fall-speeds for small crystals. If small crystals had faster fall speeds than assumed it could also reduce the increase in λ_o with distance after 30 km.

8 Summary

Observations of the variation in ice crystal microphysical size distributions in tropical anvil outflow as a function of longitudinal and transverse position is presented and compared with explicit and bulk model scheme predictions. Within the longitudinal or axial outflow region the variation in ice crystal PSD is broadly consistent with both bulk- and bin-microphysical model predictions showing, as expected, that aggregation and sedimentation are the dominant processes leading to the removal of ice crystals from

ACPD
11, 23761–23800, 2011

the cirrus cloud. However the observations also support recent modeling studies that bulk microphysical models have significant weaknesses when predicting IWC and PSD properties of extensive cirrus storm outflow from deep convective regions, probably due to mis-representation of ice particle sedimentation rates. It was also observed that ice crystal nucleation in the outflow margins was occurring, presenting as a weak *U*-shaped profile in the observed PSD parameter, λ_o, transverse to the anvil outflow. This nucleation appeared to exhibit the same habit characteristics of more typical developing high level frontal cirrus. The nucleation of new ice crystals occurred mostly well away from the parent cloud and after the anvil had been depleted of a large fraction of its ice water by sedimentation.

Based on the comparison between the observed cloud properties and predictions using the explicit and bulk microphysics models we have drawn the following conclusions:

λ_o decreases with distance from the storm, suggesting that there are increasing numbers of larger particles relative to smaller particles implying aggregation still occurs as growth by vapour diffusion would increase lambda (Mitchell, 1988). This is consistent with the CPI imagery.

The modelled aggregation efficiency that is most consistent with data is $E \sim 0.02$

For the bulk model, however, the best agreement was obtained for $E = 0.05$. Hence if using bulk models, the recommendation is to use a higher aggregation rate than for bin models.

These values of E are ~10 times higher than those used in typical Large Eddy Model simulations , which, at a temperature of $-60\,^{\circ}\mathrm{C}$, would typically be ~0.0016.

Any errors in the horizontal wind speed would change the gradient of the modelled λ_o vs. time by $u/20$ where u is the error in the true wind speed (in $\mathrm{m\,s^{-1}}$). This may alter the best fit of the aggregation efficiency by ~5 %.

Sedimentation effects were difficult to quantify. A 1-D parcel model including sedimentation effects was used to predict the change in λ_o with distance from the storm. Initially, within 30 km of the storm, a collection efficiency of $E = 0.02$ successfully

ACPD
11, 23761–23800, 2011

reproduced the observations. However, subsequently, the effects of differential crystal size sedimentation and the assumption that the size distribution of the ice crystals was initially uniform with height in the anvil became increasingly significant leading to an apparent increase in E required to explain the observations.

Acknowledgements. We would like to thank the staff of ARA who operated the Egrett aircraft during ACTIVE. We acknowledge the UK National Centre for Atmospheric Science (NCAS-UK) and the National Centre for Atmospheric Research (NCAR-USA) for providing instrumentation and technical staff. This work was funded by the UK Natural Environment Research Council. We would also like to thank P. Minnis and NASA for providing the CTH information.

References

Abbatt, J. P. D., Benz, S., Cziczo, D. J., Kanji, Z., Lohmann, U., and Möhler, O.: Solid Ammonium Sulfate Aerosols as Ice Nuclei: A Pathway for Cirrus Cloud Formation, Science, 313, 1770–1773, 2006.

Allen, G., Vaughan, G., Brunner, D., May, P. Heyes, W. Minnis, P., and Ayers, J. K.: Modulation of tropical convection by breaking Rossby waves, /Q. J. Roy. Met. Soc., 135(638), 125–137, doi:10.1002/qj.349, 2009.

Baran, A. J., Connolly, P. J., and Lee, C.: Testing an ensemble model of cirrus ice crystals using midlatitude in situ estimates of ice water content, volume extinction coefficient and the total solar optical depth, J. Quant. Spectrosc. Ra., 110, 1579–1598, 2009.

Baumgärdner, D., Jonsson, H., Dawson, W., O'Connor, D., and Newton, R.: The Cloud, Aerosol and Precipitation Spectrometer: a new instrument for cloud investigations, Atmos. Res., 59–60, 251–264, 2001.

Baker, B. and Lawson R. P.: Improvement in determination of ice water content from two-dimensional particle imagery. Part 1: image-to-mass relationships, J. Appl. Meteorol. Clim., 45, 1282–90, 2006.

Boussatson, M. P., Coquillat, S., and Chauzy, S.: A New Videosonde with a Particle Charge Measurement Device for In Situ Observation of Precipitation Particles, American Met. Soc., 21, 1519–1531, 2004.

Connolly, P. J., Saunders, C. P. R., Gallagher, M. W., Bower, K. N., Flynn, M. J., Choularton, T.

ACPD

11, 23761–23800, 2011

W., Whiteway, J., and Lawson, P.: Aircraft observations of the influence of electric fields on the aggregation of ice crystals, Quart. J. Roy. Meteor. Soc., 131, April, B, 608, 1695–1712, 2005.
Connolly P. J., Flynn M. J., Ulanowski, Z., Choularton, T. W., Gallagher, M. W., and Bower, K. N.: Calibration of the cloud particle imager probes using calibration beads and ice crystal analogs: the depth of field, J. Atmos. Ocean. Tech., 24,1860–79, 2007.
Danielson, E. F.: A dehydration mechanisms for the stratosphere, Geophys. Res. Lett., 9, 605–608, 1982.
Davis, M. H.: Two charged spherical conductors in a uniform electric field: Forces and field strength, Q. J. Mech. Appl. Math., 17, 499–511, 1964.
Donner, L. J., Seman, C. J., Soden, B. J., Hemler, R. S., Warren, J. C., Strom, J., and Liou, K.-N.: Large-scale ice clouds in the GFDL SKYHI general circulation model, J. Geophys. Res. 102, 21745–21768, 1997.
Edwards, J. M., Havemann, S., Thelen, J.-C., and Baran, A. J.: A new parametrization for the radiative properties of ice crystals: comparison with existing schemes and impact in a GCM, Atmos. Res., 83, 19–35, 2007.
Field, P. R., Heymsfeld, A. J., and Bansemer, A.: Snow size distribution parameterization for mid-latitude and tropical ice clouds, J. Atmos. Sci., 64, 4346–4365, 2007.
Francis, P. N.: Some aircraft observations of the scattering properties of ice crystals, J. Atmos. Sci., 52, 1142–54, 1995.
Gallagher, M. W., Connolly, P., Whiteway, J. R., Bower, K. N., Flynn, M. D., and Choularton, T. W.: An overview of the microphysical structure of cirrus clouds observed during EMERALD-1, Quart. J. Roy. Met. Soc. April, A, 132, 1143–1169, 2005
Gultepe, I. and Starr, D. O.: Microphysical and radiative development of a cirrus cloud during FIRE: implications for dynamical effects, Atmos. Res., 34,20, 43–52, 1994.
Heymsfield, A. J.: On measurements of small ice crystals in clouds, Geophys. Res. Lett., 34, L23812, doi:10.1029/2007GL030951, 2007.
Heymsfield, A. J., Lewis, S., Bansemer, A., Iaquinta, J., Miloshevich, L. M., Kajikawa M., Twohy, C., and Poellot, M. R.: A general approach for deriving the properties of cirrus and stratiform ice cloud particles, J. Atmos. Sci., 59, 3–29, 2002.
Lawson, R. P. and Baker, B. A., Schmitt, C. G., and Jensen, T. L.: An overview of the microphysical properties of Arctic clouds observed in May and July 1998 during FIRE ACE, J. Geophys. Res., 106, D14, 14,989–15,014, 2001.

ACPD
11, 23761–23800, 2011

Lawson, R. P. and Baker, B. A.: Improvement in determination of ice water content from two-dimensional particle imagery. Part II: Applications to collected data, J. Appl. Meteor., 45, 9, 1291–1303, 2006a.
Lawson, R. P., Baker, B. A., Zmarzly, P., O'Connor, D., Qixu Mo, Gayet, J.-F., and Shcherbakov, V.: Microphysical and optical properties of atmospheric ice crystals at South Pole station, J. Appl. Meteorol. Clim., 45, 1505–24, 2006b.
Lilly, D. K. Cirrus Outflow Dynamics, J. Atmos. Sci., 45(10), 1594–1605, 1988.
Liou, K. N. and Takano, Y.: Light scattering by non-spherical particles: remote sensing and climatic implications, Atmos. Res., 31, 271–98, 1994.
Miloshevich, L. M., Heymsfield, A. J., and Norris, P.: Microphysical measurements in cirrus clouds from ice crystal replicator sondes launched during FIRE II, 11th International Conference on Clouds and Precipitation, Montreal, Quebec, Canada, 17–21 August, 1992.
Saunders, C. P. R. and Wahab, N. M. A.: The influence of electric fields on the aggregation of ice crystals, J. Meteorol. Soc. Jpn., 53, 121–126, 1975.
Starr, D. O'C. and Cox, S. K.: Cirrus clouds. Part II: numerical experiments on the formation and maintenance of cirrus, J. Atmos. Sci, 42, 2682–2694, 1985.
Spichtinger, P. and Cziczo, D. J.: Impact of heterogeneous ice nuclei on homogeneous freezing events in cirrus clouds, J. Geophys. Res., 115, D14208, doi:10.1029/2009JD012168, 2010.
Stephens, G. L., Vane, D. G., Boain, R. J., Mace, G. G., Sassen, K., Wang, Z., Illingworth, A. J., O'Connor, E. J., Rossow, W. B., Durden, S. L., Miller, S. D., Austin, R. T., Benedetti, A., Mitrescu, C., and the CloudSat Science Team: The cloudsat mission and the a-train—a new dimension of space-based observations of clouds and precipitation, Bull Am. Meteorol. Soc., 83, 1771–90, 2002.
Takahashi, T., Tokuno, M., and De la Mar, R.: Videosonde observations of precipitation processes in equatorial cloud clusters, J. Meteor. Soc. Japan, 73, 509–534, 1995.
Vaughan, G., Schiller, C., MacKenzie, A. R., Bower, K. N., Peter, T., Schlager, H., Harris, N. R. P., and May, P. T.: Studies in a natural laboratory: High-altitude aircraft measurements around deep tropical convection., Bull. Amer. Meteorol. Soc., 88, 647–662, 2008.
Verheggen, B., Cozic, J., Weingartner, E., Bower K., Mertes, S., Connolly, P., Gallagher, M., Flynn, M., Choularton, T., and Baltensperger, U.: Aerosol partitioning between interstitial and the condensed phase in mixed phase clouds, J.Geophys. Res., 112, D23202, doi:10.1029/2007JD008714, 2007.
Whiteway, J. A., Cook, C., Gallagher, M. W., Choularton, T., Harries, J., Connolly, P.,

ACPD
11, 23761–23800, 2011

Busen, R., Bower, K., Flynn, M., May, P., Aspey, R. and Hacker, J.: Anatomy of Cirrus Clouds: Results for the Emerald airborne campaigns, Geophys. Res. Let., 31, L24102, doi:10.1029/2004GL021201, 2004.

ACPD
11, 23761–23800, 2011

Table 1. Track Longitude, Latitude and Track lengths.

Track No.	Longitude ° (core distance km)	Latitude °	Track (km)
1	129.75 *(19)*	−10.820 to −12.115	144
2	129.64 *(31)*	−12.110 to −10.970	127
3	129.31 *(67)*	−11.145 to −12.252	123
4	129.07 *(93)*	−12.239 to −11.055	132

ACPD
11, 23761–23800, 2011

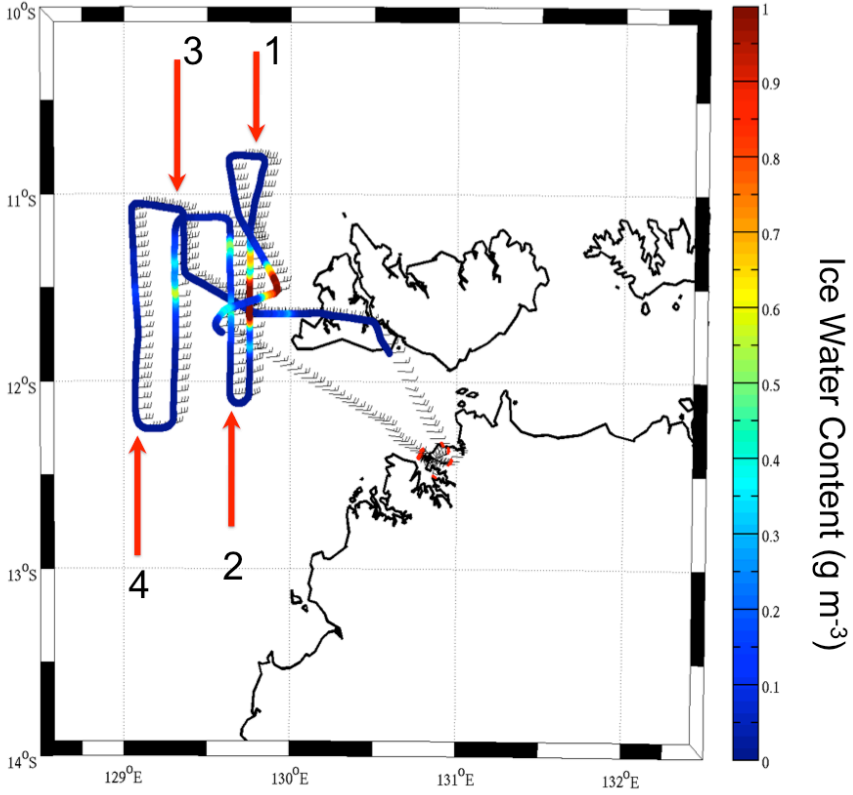

Fig. 1. Cirrus penetration flight tracks 1 to 4 during case study AE13 (9/11/2005) shown on a map of the Darwin region and the Melville and Bathhurst islands in the Beagle Gulf. Darwin city is marked. The aircraft flight tracks are colour coded according to ice water content, IWC, ($g\,m^{-3}$) (see text).

ACPD
11, 23761–23800, 2011

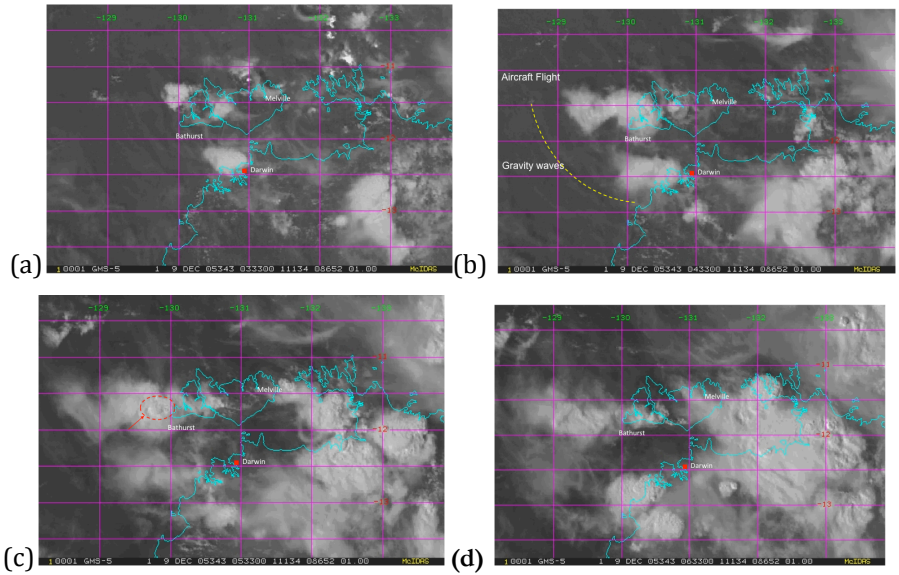

Fig. 2. MTSAT Visible images showing a Hector storm developing, north of Darwin and the cirrus outflow (see text). ACTIVE case AE13 on 9/12/2005 from 03:33–06:16 UTC. Melville and Bathurst islands are highlighted.

ACPD
11, 23761–23800, 2011

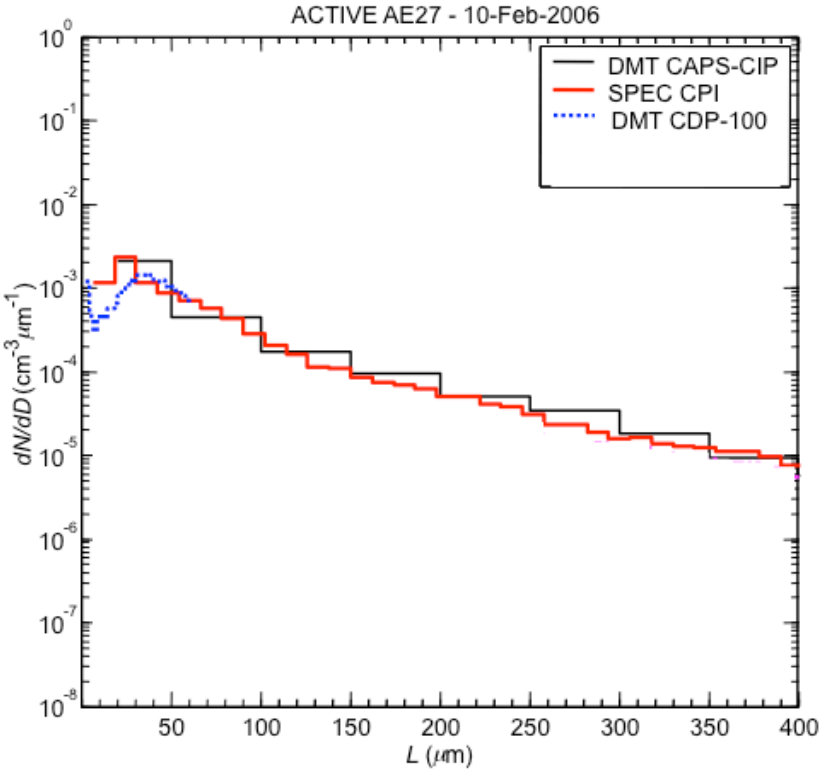

Fig. 3. Particle size distribution measurement comparison observed between the SPEC CPI and DMT CAPS-CIP instruments for **(a)** Particle size range 10< L <400 µm and **(b)** 10< L <1800 µm. Also shown is the PSD in the size range 2< D_p <62 µm measured by a Mie scattering spectrometer (DMT CDP-100).

ACPD
11, 23761–23800, 2011

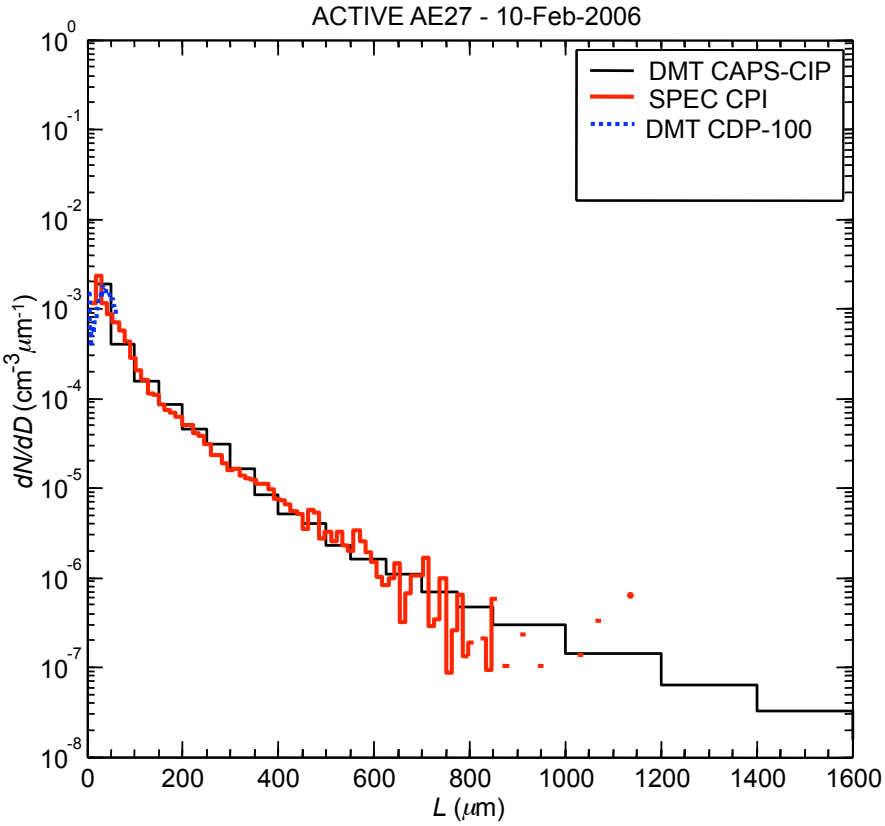

Fig. 4. As Fig. 3, but for particle size range, 10< L <1800 µm. Also shown is the PSD in the size range As Fig. 3, but for particle size range, 10< L <1800 µm. Also shown is the PSD in the size range 2< D_p62 µm measured by a Mie scattering spectrometer (DMT CDP-100).

ACPD
11, 23761–23800, 2011

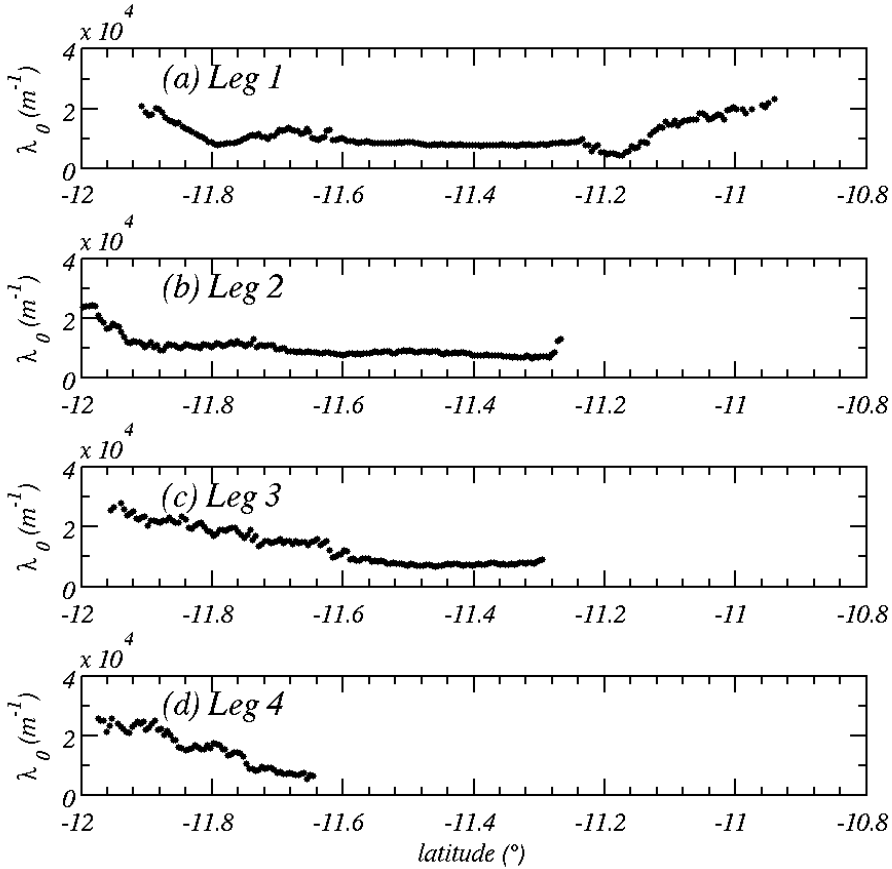

Fig. 5. IWC ($g\,m^{-3}$) determined by CIP across each flight leg 1–4, **(a)**–**(d)** as a function of increasing distance from the storm centre. There is a general decrease in IWC with distance as well significant lateral shift in core outflow.

ACPD
11, 23761–23800, 2011

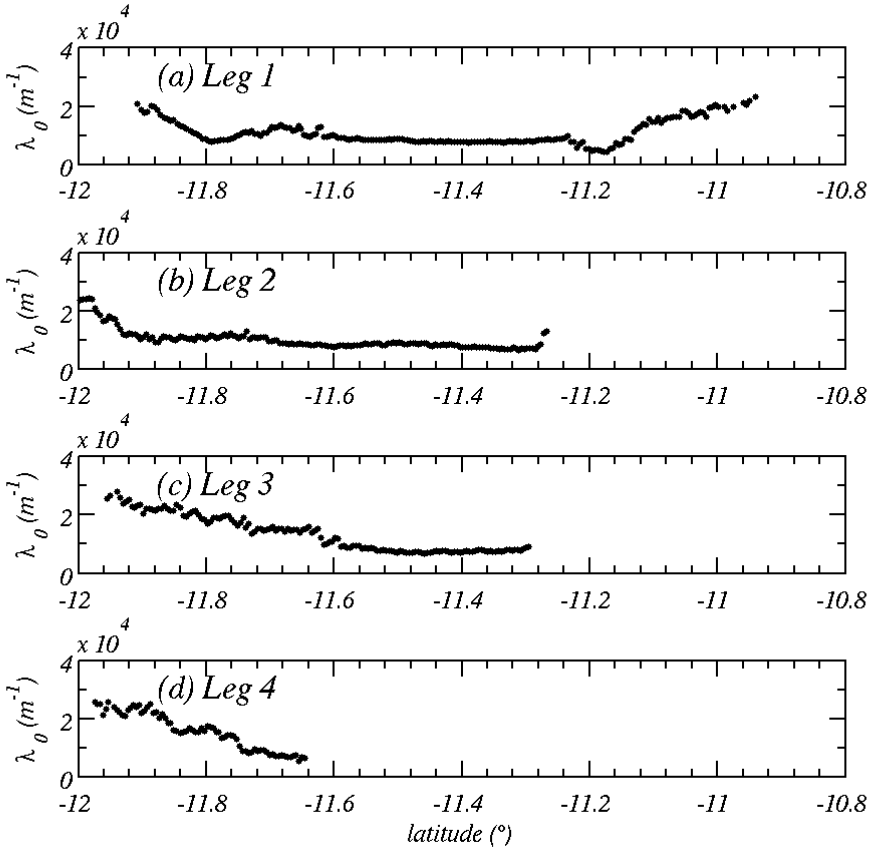

Fig. 6. The derived λ_0 (cm^{-1}) for each leg as a function of latitude with each flight as a function of increasing distance from the storm **(a)–(d)**. There is a general decrease in λ_0 with distance from the storm.

ACPD
11, 23761–23800, 2011

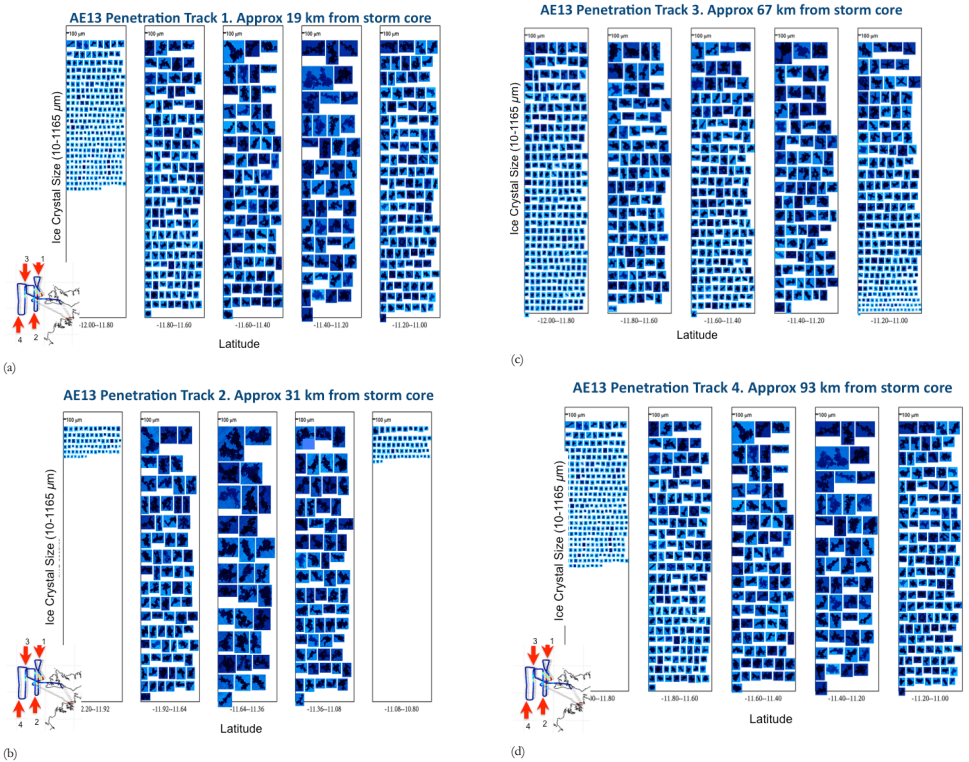

Fig. 7. CPI unprocessed images recorded during cloud penetrations 1 to 4 perpendicular to the storm outflow with increasing distances, 19, 31, 67 and 93 km, figures **(a)** to **(d)** respectively, from the storm. The crystal images observed are represented in a matrix with the horizontal axis split into 5 latitude bands of width: 0.2°, perpendicular to the outflow direction. The vertical axis is sorted as a function of the maximum ice crystal size (from 5 to ~1120 μm) observed in each latitude bin. The size scale at the top of each column represents 100 μm.

ACPD
11, 23761–23800, 2011

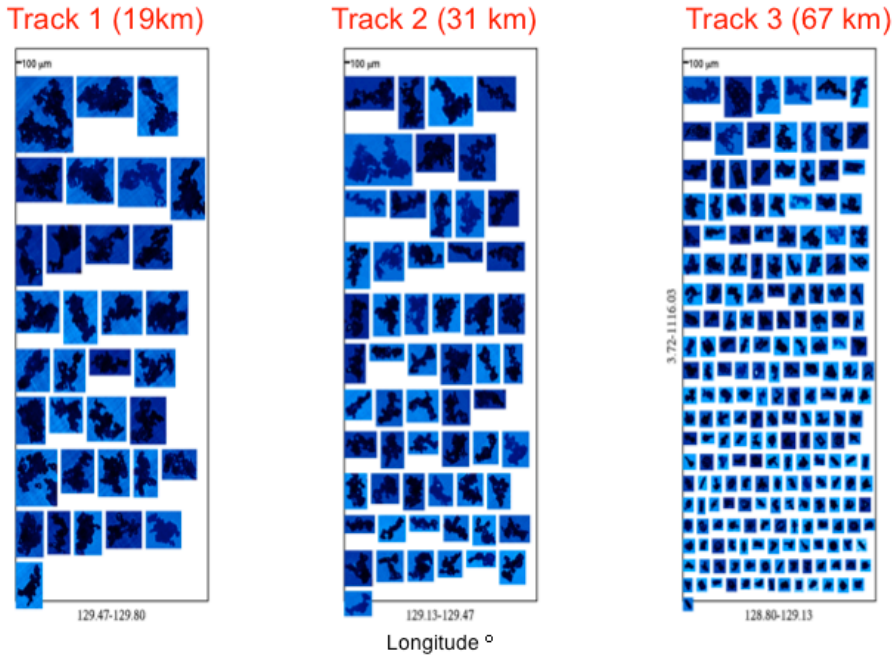

Fig. 8. Ice crystal habits and sizes along the centre-line of the storm outflow during AE13 at 19, 31 and 67 km respectively showing recovery in n_o and reduction in aggregate contributions.

ACPD
11, 23761–23800, 2011

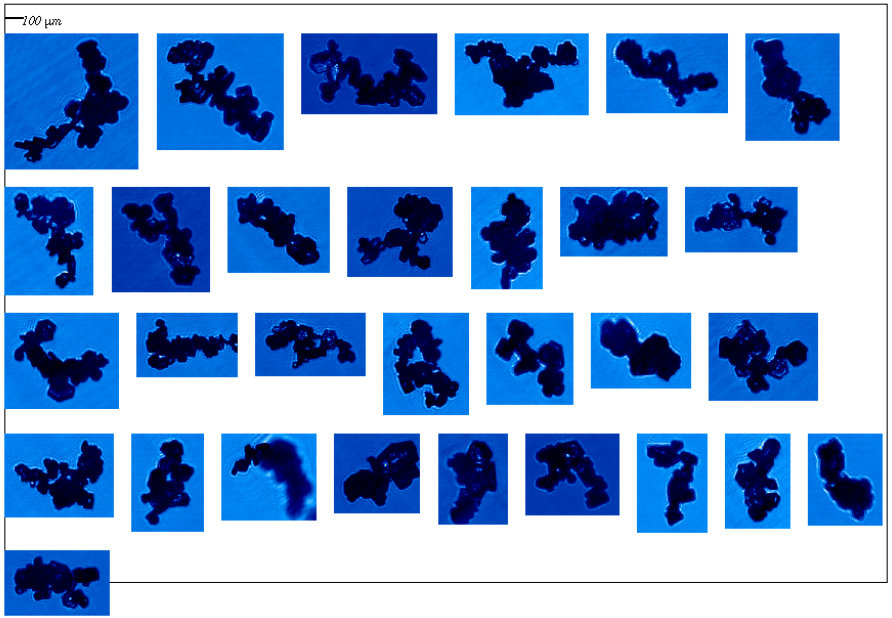

Fig. 9. Close up view of typical complex chain aggregates of hexagonal plates observed within a Hector storm outflow (temperatures $T < -50\,^{\circ}\mathrm{C}$) during the ACTIVE-2 experiment, Connolly et al. (2007).

ACPD
11, 23761–23800, 2011

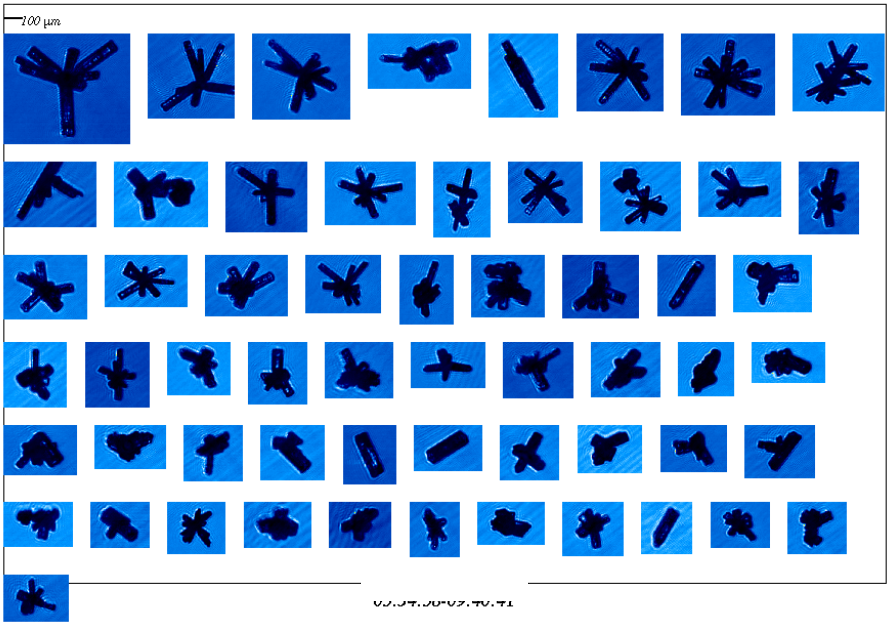

Fig. 10. Ice crystal habits observed in high-level frontal cirrus, at temperatures $T < -40\,^{\circ}C$, over Adelaide, Australia, during the EMERALD-1 experiment, Gallagher et al. (2005). Habits presented as mainly pristine bullet rosettes.

ACPD
11, 23761–23800, 2011

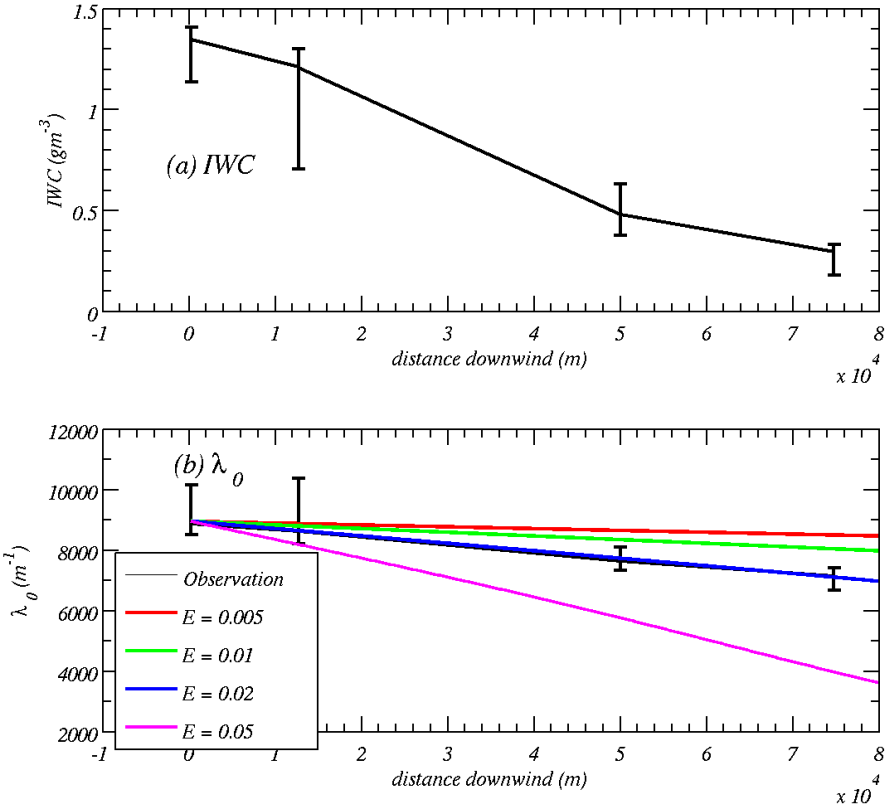

Fig. 11. (a); The IWC inferred from the CIP instrument as a function of distance from the main storm; **(b)**; the λ_o parameter as a function of distance from the main storm and as a function of aggregation efficiency, E, predicted by the model and compared to the λ_o derived from CIP measurements.

ACPD
11, 23761–23800, 2011

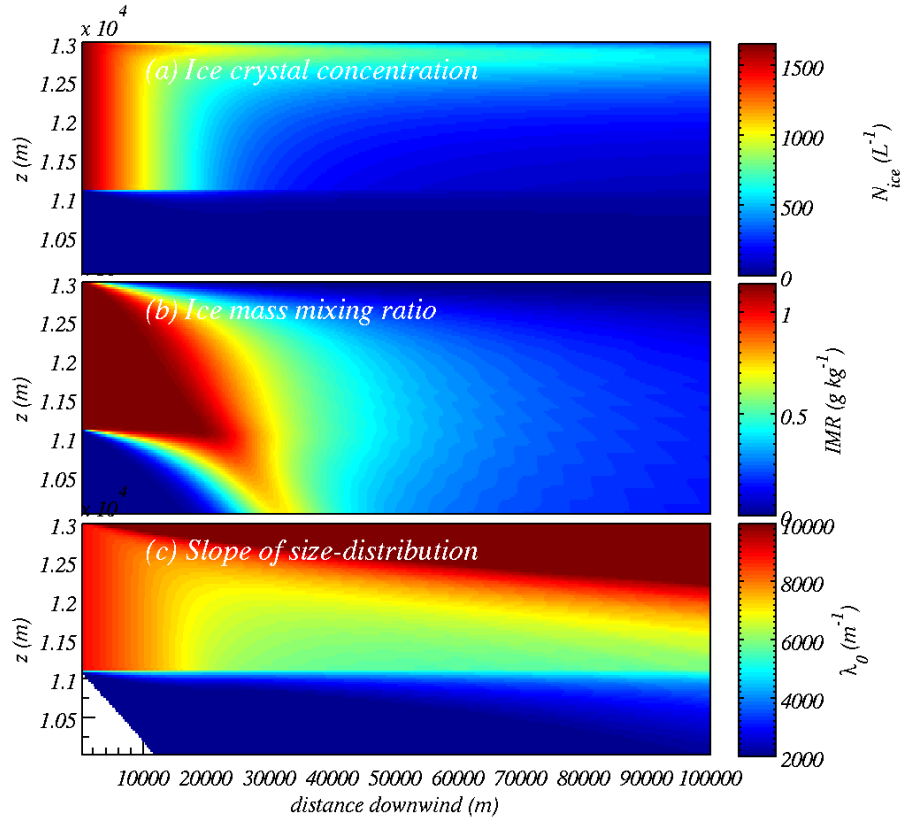

Fig. 12. Contour plots of a typical output from the sedimentation/aggregation model. **(a)** shows the time-height evolution of ice crystal number concentration, $N(L^{-1})$; **(b)** shows the time-height evolution of ice mixing ratio (IMR, g kg^{-1}); and **(c)** shows the time-height evolution of the slope of the distribution λ_o (m^{-1}).

ACPD
11, 23761–23800, 2011

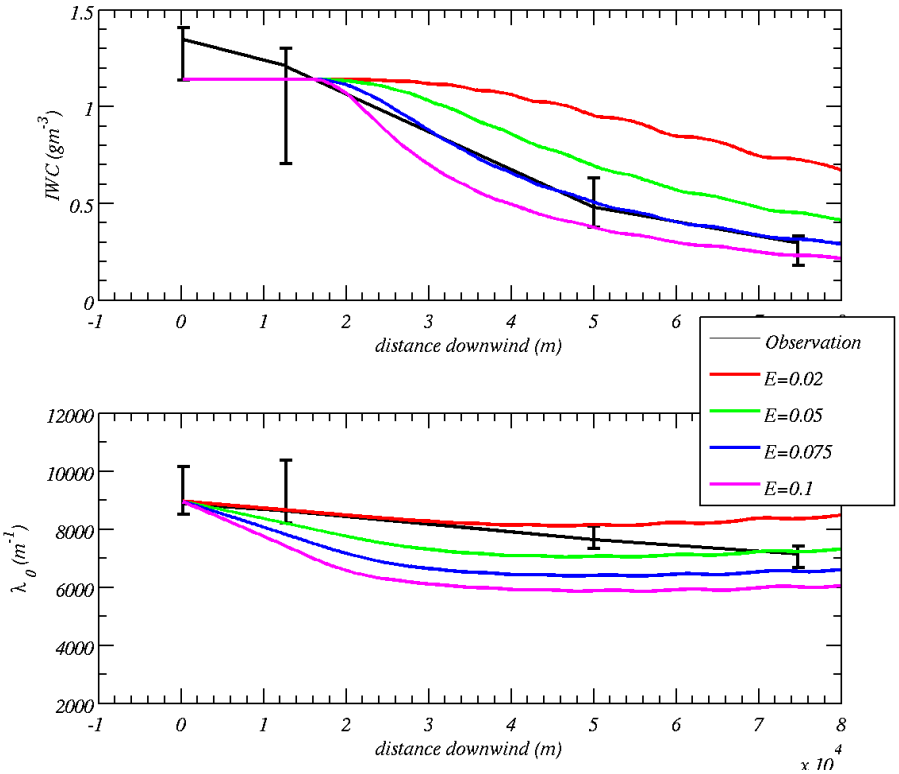

Fig. 13. (a) The IWC (g m^{-3}) inferred from the CIP instrument as a function of distance from the main storm and that predicted with the sedimentation model for differing collection efficiencies E = 0.02, 0.05, 0.075, and 0.1; **(b)** Observed and predicted λ_o (m^{-1}) as a function of distance from the main storm.

ACPD
11, 23761–23800, 2011